Supplementary Information for

Tailoring I-rich argyrodite sulfides via low-energy mechanical alloying for all-solid-state Li-metal batteries

Young Jung Kim,[ab] Sahn Nahm,[b] Jae Jin Kim,[a] Jong-Ho Lee,*[a] and Hyoungchul Kim*[c]

[a]*Center for Hydrogen Energy Materials, Korea Institute of Science and Technology, 5 Hwarang-ro 14-gil, Seongbuk-gu, Seoul 02792, Republic of Korea*

[b]*Department of Materials Science and Engineering, Korea University, 145 Anam-ro, Seongbuk-gu, Seoul 02841, Republic of Korea*

[c]*Department of Mechanical and System Design Engineering, Hongik University, 94 Wausan-ro, Mapo-gu, Seoul 04066, Republic of Korea*

*Corresponding authors. E-mail address: jongho@kist.re.kr (J.-H. Lee),

hyoungchul@hongik.ac.kr (H. Kim)

Experimental section

Preparation of solid electrolytes (SEs).

$Li_{5.6}PS_{4.6}Cl_{1.4-x}I_x$ ($0 \leq x \leq 1.4$; $Cl_{1.4-x}I_x$) SEs were synthesized via mechanical alloying. Stoichiometric amounts of Li_2S (99.98%, Sigma-Aldrich), P_2S_5 (99%, Sigma-Aldrich), LiCl (99%, Sigma-Aldrich), and LiI (99%, Sigma-Aldrich) were mixed in a 6.75 g batch and loaded into a zirconia jar with 135 g of zirconia balls (diameter: 3 mm). The mixtures were milled for 12 h using a planetary machine (Pulverisette 5 Premium Line, Fritsch) under two different conditions: low-energy mechanical alloying (LMA) at 550 rpm and high-energy mechanical alloying (HMA) at 700 rpm. They correspond to centrifugal accelerations of approximately 30 g-force (GF) and 49 GF, respectively. Here, the GF was calculated from the centrifugal acceleration normalized by gravitational acceleration (g = 9.8 m s^{-2}), using the effective rotation radius of the main disk (R = 0.089 m). After milling, the SEs were sieved to collect particles smaller than 100 μm.

$$GF = \frac{(rpm \times \frac{2\pi}{60})^2 \times R}{g}$$

Characterization of SEs

The crystal structures of $Cl_{1.4-x}I_x$ SEs were examined using X-ray diffraction (XRD) using a powder diffractometer (D8 Advance, Bruker) with Cu Kα radiation (λ = 1.542 Å) in the 2θ range of 10–60° at a scan rate of 2.0° min^{-1}. The powder was spread evenly on the holder and sealed under Ar using a Kapton film to prevent air exposure. Li-ion conductivities (σ_{Li}) were measured using an electrochemical analyzer (EnergyLab XM, Solartron). Rietveld refinement of the obtained XRD data were performed using the TOPAS V5 software (Bruker). The fundamental

parameters approach was applied for XRD pattern modeling. During the refinement, the atomic positions, excluding Li and the occupancies of the anion sites (S, Cl, and I) were treated as adjustable parameters. The occupancies of Cl and I at the Wyckoff 4*a* and 4*c* sites were refined with the constraint that the total occupancy at each site was set to unity. To analyze the crystal size of the material, Pawley refinement was utilized. The process extracts the unit cell parameters and atomic positions with high precision. The fitting process included adjusting the background and peak profile shapes to obtain the best fit to the observed data. The reliability of the refined structural model was evaluated based on the R_{wp} and R_{exp} fit indicators, as well as the goodness-of-fit (GoF).

The crystal structure of the samples was examined using transmission electron microscopy (TEM; Tecnai G2, FEI) at an accelerating voltage of 200 kV. The specimens were dispersed onto carbon-coated copper TEM grids. To prevent air exposure during transfer, a double-tilt vacuum transfer holder (Model 648, Gatan) was employed, maintaining vacuum from initial sample preparation to TEM loading.

0.1 g of SE sample was pressed into a pellet (diameter: 6 mm) at 504 MPa. Impedance spectra were collected over 1×10^{6} –1×10^{-1} Hz with an AC amplitude of 50 mV. The bulk resistance (R_{Bulk}) was determined from the high-frequency intercepts of the Nyquist plots. σ_{Li} was calculated using the measured R_{Bulk}, pellet thickness (t), and area (A):

$$\sigma_{Li} = \frac{t}{R_{Bulk}A}$$

Mechanical properties of $Cl_{1.4-x}I_x$ were measured via ultrasonic pulse-echo techniques. A 0.1 g sample was compressed into a pellet (diameter: 10 mm) at 454 MPa. To prevent air exposure, the pellets were enclosed in a 0.2 mm-thick aluminum foil holder and sealed using a vacuum sealer. Longitudinal (V_L) and shear (V_S) wave sound velocities were obtained using

transducers (A127S-RM, V154-RM, Olympus) driven by an ultrasonic pulse/receiver (5072PR, Olympus). Using the apparent density (ρ), elastic modulus (E), shear modulus (G), bulk modulus (B), and Poisson's ratio (v) were calculated. All measurements were conducted in a sealed chamber to prevent oxidation, following a procedure reported in the literature.[1,2]

$$v = \rho \frac{(V_L^2 - 2V_S^2)}{(2V_L^2 - 2V_S^2)}$$

$$E = 3\rho V_S^2 \frac{(V_L^2 - \frac{4}{3}V_S^2)}{(V_L^2 - V_S^2)}$$

$$G = \rho V_S^2$$

$$B = \rho \frac{(V_L^2 - \frac{4}{3}V_S^2)}{(V_L^2 - V_S^2)}$$

To evaluate interfacial stability between Li metal and $Cl_{1.4-x}I_x$ SEs, critical current density (CCD) tests were performed using symmetric Li/$Cl_{1.4-x}I_x$/ Li cells. All the electrochemical measurements were performed using a potentiostat/galvanostat (SP-300, BioLogic). A 0.15 g sample of $Cl_{1.4-x}I_x$ SE was pressed into a pellet (diameter: 10 mm) under 555 MPa, and 9 mm Li metal foils (diameter: 9 mm) were placed on both sides. The cell was assembled at a constant torque of 2.3 N-m. CCD tests were performed with stepwise current increments of 0.1 mA cm^{-2}, with 1 h plating/stripping per step.

Fabrication of all-solid-state Li metal batteries (ASSLMBs).

The cathode layer (CL) was fabricated as a dry electrode sheet using the shear stress process. 60 vol% of $LiNbO_3$-coated $LiNi_{0.8}Co_{0.1}Mn_{0.1}O_2$ (Nb-NCM811) and 40 vol% of $Li_{5.4}PS_{4.4}Cl_{0.8}Br_{0.8}$ were milled at 20,000 rpm for 160 s using a portable mill. Vapor-grown carbon fiber (2 wt%; VGCF) were then added and milled at 20000 rpm for 20 s. Finally, a 0.9 wt%

polytetrafluoroethylene (PTFE) binder was incorporated and mixed under identical conditions. The resulting mixture was manually ground for 10 min into a dough-like form and pressed under shear stress via a roll-to-roll machine to form sheets thinner than 100 μm. All processes were conducted in a dry room with a dew point below −45 °C. For assembly ASSLMBs, 90 mg of $Cl_{1.4-x}I_x$ SEs was pressed into a pellet (diameter: 10 mm) at 136 MPa for 2 min. A 70 μm-thick CL sheet (diameter: 10 mm) was stacked on one side and compressed to 442 MPa for 2 min. A 200 μm-thick Li metal foil (diameter: 9 mm) was polished to remove surface oxides before being placed in contact with the electrolyte layer (EL), followed by a 10 μm-thick Ni foil current collector (diameter: 10 mm). The assembled ASSLMBs were clamped under a 2.3 N-m torque in a triaxial mold to ensure stable mechanical contact. All the fabrication steps were performed in an Ar-filled glovebox (O_2 < 0.5 ppm).

Electrochemical performance of ASSLMBs.

ASSLMBs were sealed in Ar-filled containers and tested at 25 °C using an incubator to prevent air exposure. Galvanostatic cycling was conducted using a battery tester (Model 4300K, Maccor) between 2.5 and 4.25 V (*vs*. Li^+/Li). A formation step at 0.05C was followed by cycling at 0.25C, based on a cathode active material capacity of 200 mAh g^{-1}. Long-term cycling was performed for up to 100 cycles at 0.25 C and 250 cycles at 1 C, with CE calculated from charge-discharge capacity ratios. Rate-capability tests were performed sequentially at 0.05, 0.25, 0.5, and 1C, with four charge-discharge cycles per step, followed by recovery at 0.05C to verify reversible capacity retention.

Characterization of ASSLMBs.

The cross-sections of the as-fabricated ASSLMBs were examined using scanning electron microscopy (SEM; Regulus 8230, Hitachi). Samples were cut to expose cross-sections and transferred to the SEM chamber using a vacuum transfer holder to prevent atmospheric exposure. Imaging was performed at 10-15 kV using both secondary and backscattered electron (BSE) modes to resolve morphology and compositional contrast. Distinct layers corresponding to the cathode, SE, and anode regions were clearly observed in the BSE mode. For more detailed interfacial analysis, particularly at the Li metal-SE interface (LSI), Focused ion beam (FIB)-SEM (Helios 5 Hydra UX, Thermo Fisher Scientific) was used. Milling was conducted using a Xe plasma ion source at an accelerating voltage of 30 kV and a beam current of 2.5 μA under room temperature. The milled cross-sections were observed in SEM mode using voltage of 5 kV and a current of 0.4 nA to minimize beam-induced damage and enhance interfacial contrast.

For the electrochemical impedance spectroscopy (EIS) tests, charged ASSLMBs were analyzed using an electrochemical analyzer (EnergyLab XM, Solartron) over a frequency range of 10^{6}–10^{-1} Hz with an amplitude of 50 mV. The measurements were conducted every 20 cycles for up to 100 cycles. The obtained spectra were fitted using an equivalent circuit model in ZView (Scribner Associates) within 5×10^{5}–5×10^{-1} Hz. The circuit comprises R_{Bulk}, $R_{\text{I-1}}$, $R_{\text{I-2}}$, and $R_{\text{I-3}}$, each modeled as a parallel resistance-capacitance (R–C) circuit.[3,4] CPE parameters (CPE-T, CPE-P) were adjusted to maintain consistent fitting order; CPE-P values were constrained between 0.5 and 1 to account for non-ideal interfacial behavior. A Warburg impedance element was included to reflect the contributions of the Li-ion diffusion.

To investigate the interfacial chemical degradation of the SEs before and after cycling, X-ray photoelectron spectroscopy (XPS) measurements were conducted using a spectrometer

(Nexas, Thermo Fisher Scientific) equipped with an Al Kα source at 1486.6 eV. Spectra for the S 2*p*, P 2*p*, and I 3*d* elements were recorded for both as-fabricated and cycled cells to analyze redox-induced degradation at the Li metal interface. Depth profiling analysis was additionally performed as a function of etching time. Ar^+ ion sputtering was applied at an ion energy of 2 kV over a raster area of 1 mm × 1 mm. The sputtering rate was approximately 0.5 nm s^{-1}, calibrated based on a SiO_2 reference sample. Samples were attached on a sample holder in a dry Ar-filled glovebox and transferred to a chamber using a vacuum transfer vessel to avoid air exposure. Before data fitting, all spectra were calibrated to the C 1*s* standard peak at 284.8 eV. The obtained spectra were deconvoluted using MultiPak software (ULVAC-PHI Inc.).

Time-of-flight secondary ion mass spectrometry (TOF-SIMS; M6, IONTOF GmbH) was conducted to analyze the interfacial degradation of cells. The analysis was performed in negative ion mode using a Bi_3^+ primary ion source at 30 keV and a current condition of 0.6 pA. The analysis area was set to 100 μm × 100 μm, and the spectrometry mode was used to ensure high mass resolution and detailed mass spectra data. The data were evaluated by software (SurfaceLab 7.5, IONTOF GmbH) and normalized to the total ion signal for reliable fragment comparison.

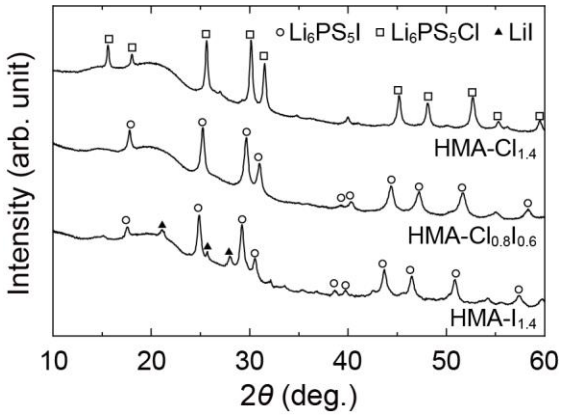

Fig. S1 XRD patterns of HMA-$Cl_{1.4-x}I_x$ ($0 \leq x \leq 1.4$) SEs. References XRD patterns of Li_6PS_5Cl (ICSD No. 418490) and Li_6PS_5I (ICSD No. 421083) are also shown.

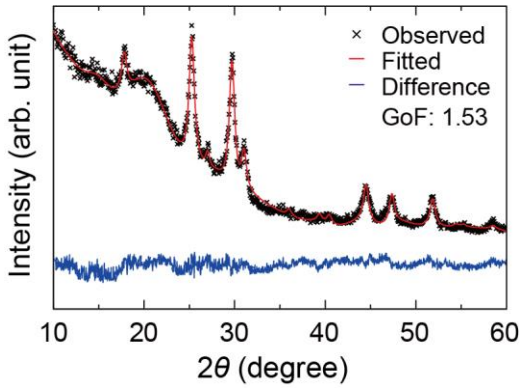

Fig. S2 Rietveld refinement of the XRD pattern for the LMA-$Cl_{0.8}I_{0.6}$. The refinement yields a GoF value of 1.53, indicating reliable structural fitting and phase identification.

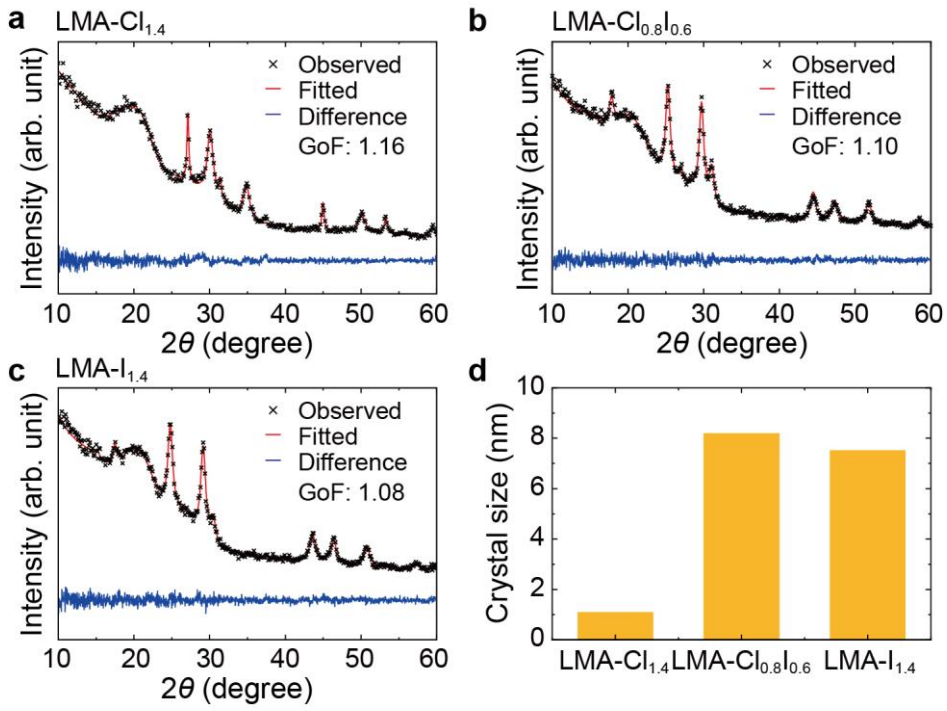

Fig. S3 Pawley refinement results of the XRD patterns for (a) LMA-$Cl_{1.4}$, (b) LMA-$Cl_{0.8}I_{0.6}$, and (c) LMA-$I_{1.4}$. The refinements converged with GoF values of 1.16, 1.10, and 1.08, respectively, confirming reliable peak fitting. (d) Comparison of their crystal sizes estimated from the Pawley refinement results.

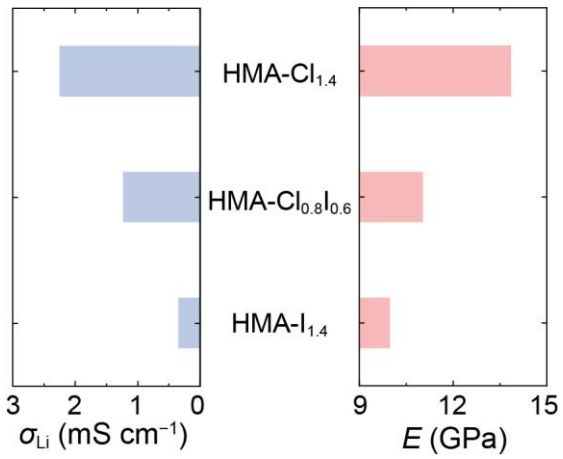

Fig. S4 Comparison of σ_{Li} and E in the HMA-$Cl_{1.4-x}I_x$ samples.

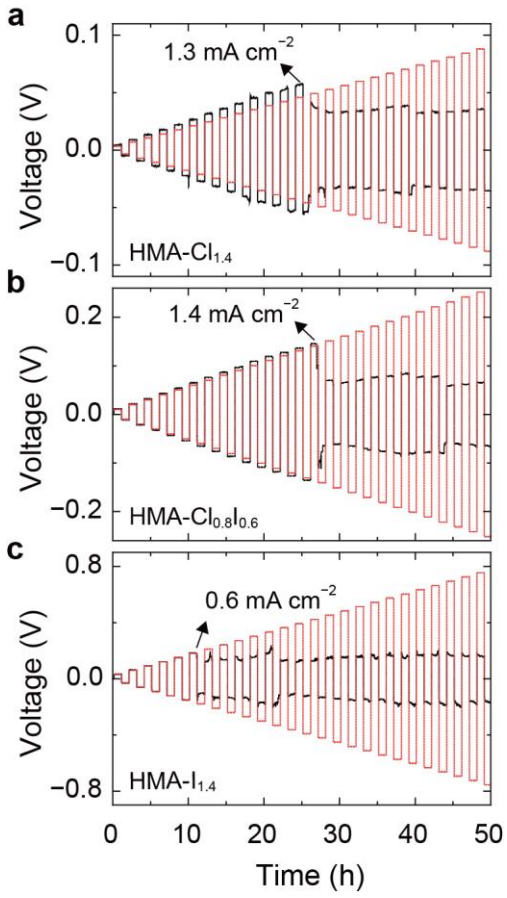

Fig. S5 The CCD profiles of HMA-$Cl_{1.4-x}I_x$ samples: (a) HMA-$Cl_{1.4}$, (b) HMA-$Cl_{0.8}I_{0.6}$, and (c) HMA-$I_{1.4}$. Step size for the current density increase was 0.1 mA cm^{-2} for the time-constant mode.

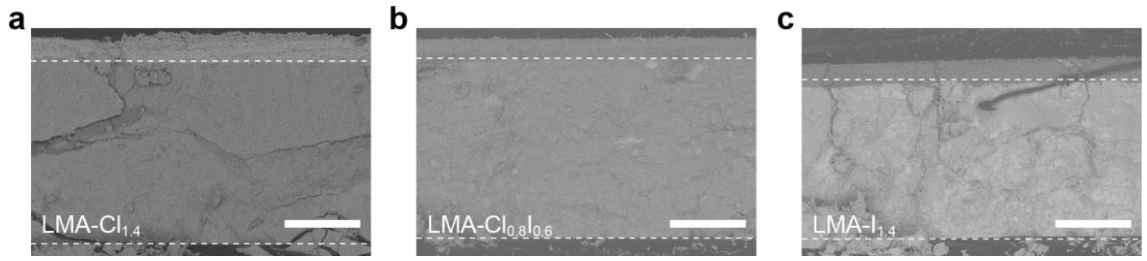

Fig. S6 Cross-sectional SEM images of as-fabricated LMA-$Cl_{1.4-x}I_x$ cells: (a) LMA-$Cl_{1.4}$. (b) LMA-$Cl_{0.8}I_{0.6}$, and (c) LMA-$I_{1.4}$. All scale bars correspond to 200 μm.

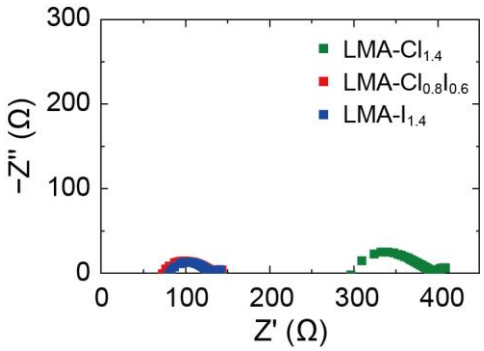

Fig. S7 The first-cycle impedance spectra of LMA-$Cl_{1.4-x}I_x$ cells at 0.05C.

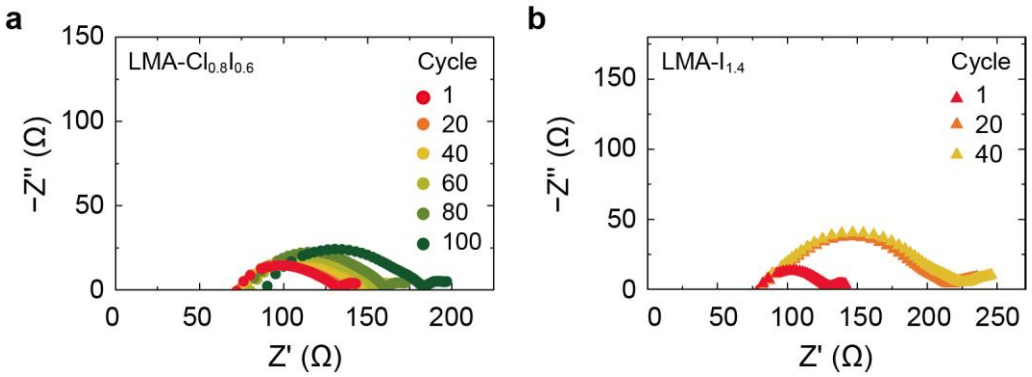

Fig. S8 The measured impedance spectra of (a) LMA-$Cl_{0.8}I_{0.6}$ and (b) LMA-$I_{1.4}$ cells during long-term cycling at 0.25C.

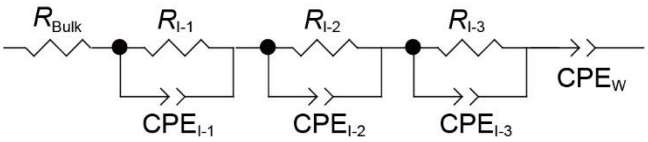

Fig. S9 An equivalent circuit model consisting of bulk resistance of SE (R_{Bulk}), grain boundary resistance of SE (R_{I-1}), interfacial resistance of cathode-SE (R_{I-2}), and interfacial resistance of Li metal-SE (R_{I-3}).

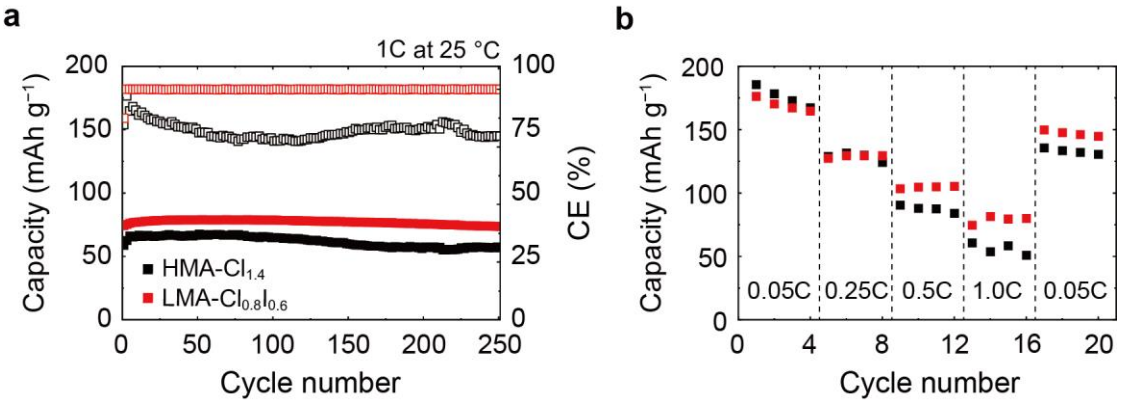

Fig. S10 Comparison of the HMA-$Cl_{1.4}$ and LMA-$Cl_{0.8}I_{0.6}$ cells. (a) Variations in discharge capacity and Coulombic efficiency (CE) during long-term cycling at 1C. Filled and open symbols represent capacity and CE, respectively. (b) Rate capability at 0.05, 0.25, 0.5, and 1.0C. All cells were maintained at 25 °C.

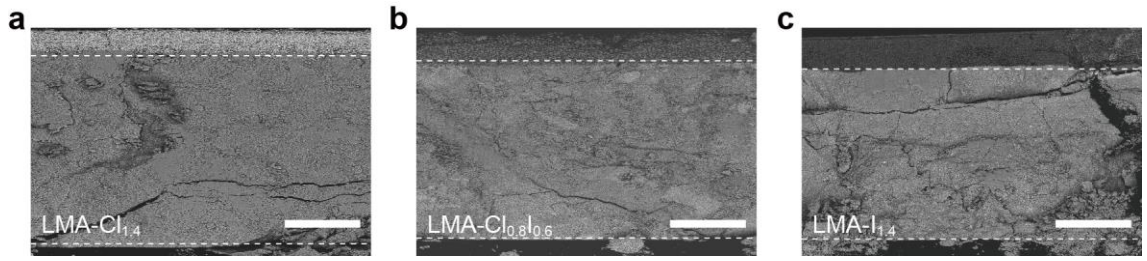

Fig. S11 Cross-sectional SEM images of after-cycling cells with (a) LMA-$Cl_{1.4}$, (b) LMA-$Cl_{0.8}I_{0.6}$, and (c) LMA-$I_{1.4}$. All scale bars correspond to 200 μm.

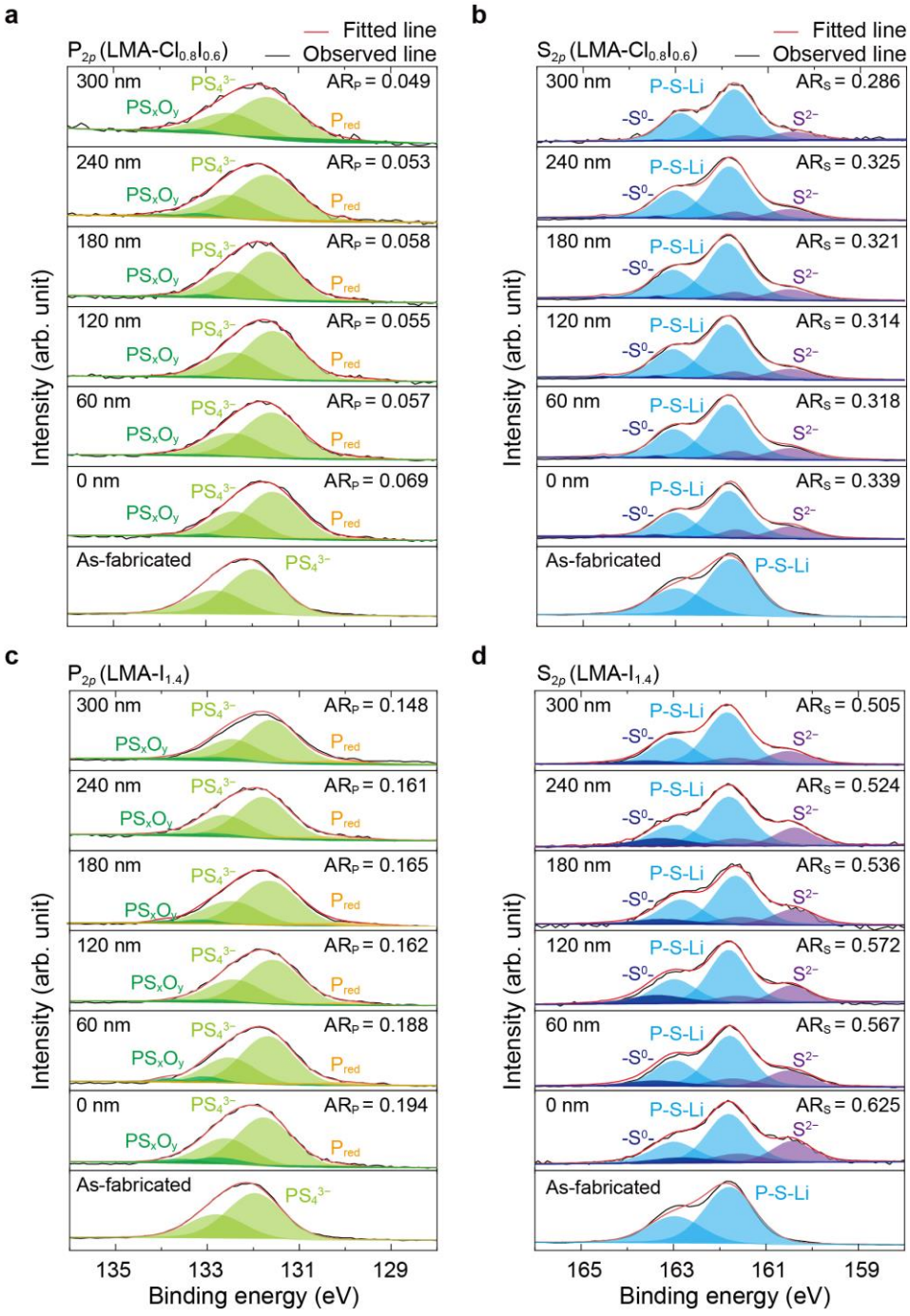

Fig. S12 XPS depth profiling results of (a) P 2*p* and (b) S 2*p* spectra for as-fabricated and after-cycling states. The sputtering depth (0–300 nm) corresponds to the distance from LSI.

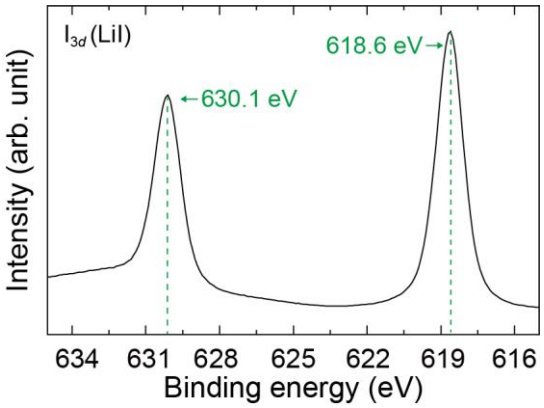

Fig. S13 A XPS spectrum of LiI in the I 3*d* region. Two peaks observed at 618.6 eV and 630.1 eV (green) were used as reference binding energies for identifying LiI formed at the interface after cycling. The binding energies of the I 3*d* doublet are consistent with reported literature.[5]

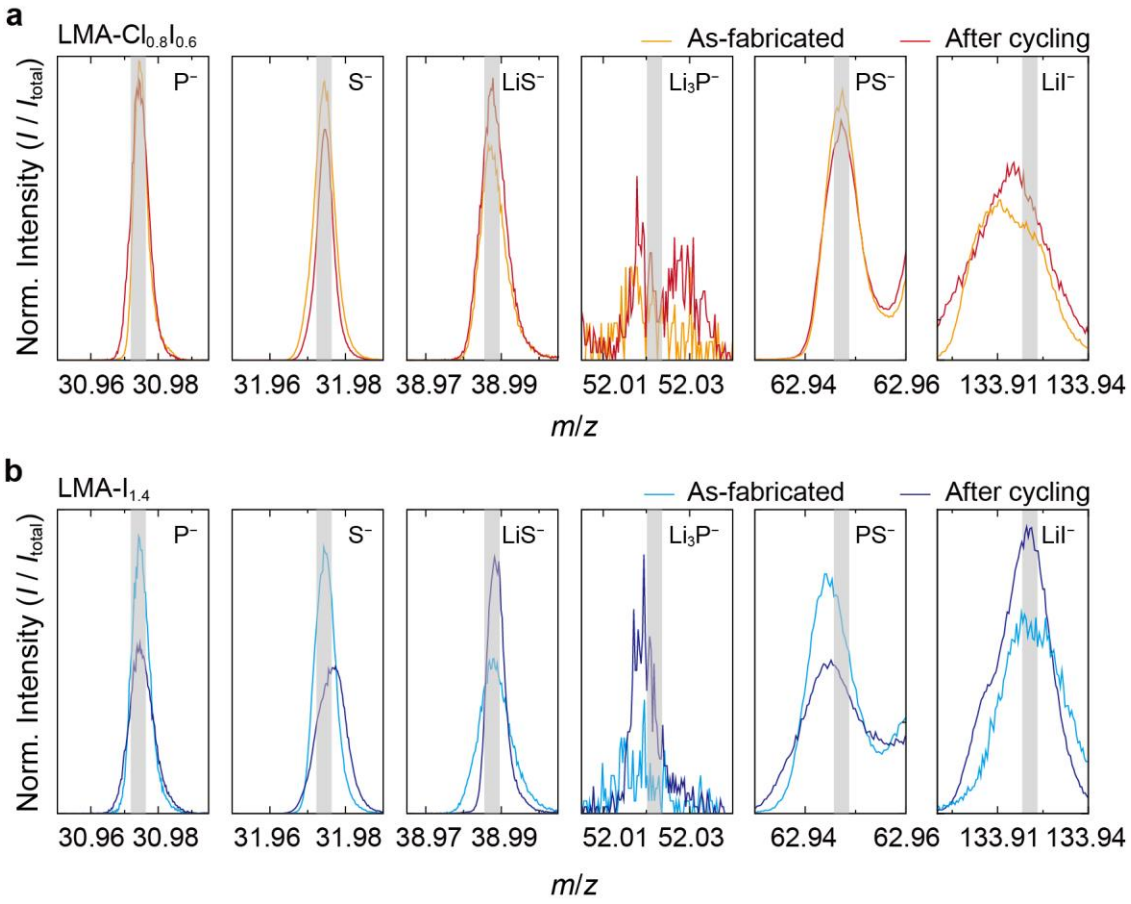

Fig. S14 TOF-SIMS spectra of representative negative fragments of (a) LMA-$Cl_{0.8}I_{0.6}$ and (b) LMA-$I_{1.4}$ in the as-fabricated and after-cycling states. For LMA-$Cl_{0.8}I_{0.6}$, the as-fabricated and after-cycling spectra are shown in orange and red, respectively. For LMA-$I_{1.4}$, the as-fabricated and after-cycling spectra are shown in cyan and purple, respectively. Normalized intensities are shown within selected *m*/*z* regions (gray region).

Table S1. Calculated G-force milling energy at different rotational speeds of the main disk. The effective diameter of the main disk was fixed at 0.089 m.

Rotational speed of main disk (rpm)	Effective diameter of main disk (m)	G-force milling energy (GF)	Notes
550	0.089	30	This work LMA
600	0.089	36	
650	0.089	42	
700	0.089	49	This work HMA
750	0.089	56	
800	0.089	64	

Table S2. Detailed crystallographic information of LMA-$Cl_{0.8}I_{0.6}$ obtained from the Rietveld refinement. B_{eq} refers to the isotropic temperature factor.

Atom	Site	Fractional atomic coordinates			Occupancy	B_{eq} (Å^2)
		x	*y*	*z*		
Li	48*h*	0.3142	0.6858	0.0148	0.5252	2.6070
Li	16*e*	0.1370	0.1370	0.1370	0.0090	2.6070
Li	24*g*	0.0250	0.2500	0.7500	0.0090	2.6070
Li	48*h*	0.4859	−0.0141	0.1945	0.0122	2.6070
P	4*b*	0.0000	0.0000	0.5000	1.0000	0.8734
S	16*e*	0.1200	−0.1200	0.6200	1.0000	1.8410
S	4*a*	0.0000	0.0000	0.0000	0.3744	2.1020
Cl	4*a*	0.0000	0.0000	0.0000	0.1992	2.1020
I	4*a*	0.0000	0.0000	0.0000	0.4268	2.1020
S	4*c*	0.2500	0.2500	0.7500	0.1082	3.4000
Cl	4c	0.2500	0.2500	0.7500	0.2517	3.4000
I	4c	0.2500	0.2500	0.7500	0.4723	3.4000

Table S3. Summary of previously reported I-based argyrodite SEs. MM, HT, SS refer to mechanical milling, heat treatment, and solid-state synthesis, respectively.

Material	Primary phase	Process	σ_{Li} (mS cm^{-1})	CCD (mA cm^{-2})	Anode material	Role in a full cell	Ref.
$Li_{5.6}PS_{4.6}Cl_{0.8}I_{0.6}$	Li_6PS_5I	MM	2.44	1.6	Li	SE	This work
$Li_{5.6}PS_{4.6}I_{1.4}$	Li_6PS_5I	MM	2.04	-	Li	Interlayer	6
$Li_{6.6}P_{0.8}Sn_{0.2}S_5I_{0.6}Cl_{0.4}$	Li_6PS_5I	MM	0.96	0.8	Li-In	SE	7
$Li_6PS_5F_{0.25}I_{0.75}$	Li_6PS_5I	SS	0.35	-	Li	SE	8
$Li_{6.24}P_{0.823}Sn_{0.177}S_{4.58}I_{0.9}$	Li_6PS_5I	MM + HT	0.35	-	Li	Interlayer	9
$Li_{5.6}PS_{4.6}I_{1.4}$	Li_6PS_5I	MM	0.31	-	Li-In	SE	10
Li_6PS_5I	Li_6PS_5I	MM	0.21	-	Li-In	SE	11
$Li_{5.4}PS_{4.4}Cl_{1.4}I_{0.2}$	Li_6PS_5Cl	MM + HT	11.49	1.35	Li	SE	12
$Li_{5.6}PS_{4.6}Cl_{1.3}I_{0.1}$	Li_6PS_5Cl	MM + HT	10.45	1.74	Li	SE	13
$Li_6PS_5Cl_{1.45}I_{0.15}$	Li_6PS_5Cl	MM + HT	5.7	1.65	Li-In	SE	14
$Li_6PS_{4.8}O_{0.2}Cl$-5 wt.% I_2	Li_6PS_5Cl	MM + HT	3.78	21	Li	SE	15
$Li_6PSCl_{0.7}I_{0.3}$	Li_6PS_5Cl	MM + HT	2.33	-	Li-In	SE	16
$Li_{10.1}P_{2.95}S_{0.05}S_{12}I$	$Li_{10}PS_{12}I$	MM + HT	5.9	1	Li	SE	17
$Li_7P_2S_8Br_{0.5}I_{0.5}$	$Li_7P_2S_8I$	MM + HT	5.9	1.4	Li-In	SE	18
$Li_7P_2S_8Cl_{0.5}I_{0.5}$	$Li_7P_2S_8I$	MM + HT	3.08	-	Li	SE	19
$Li_6P_2S_8I$	$Li_6P_2S_8I$	MM + HT	1.00	-	In	SE	20

Table S4. Individual fitting component values over the cycle number obtained from EIS results.

	LMA-$Cl_{0.8}I_{0.6}$						LMA-$I_{1.4}$			LMA-Cl1.4
Cycle number	1	20	40	60	80	100	1	20	40	1
R_{Bulk} (Ω)	73.26	73.31	78.37	82.64	82.65	92.51	79.46	84.43	86.03	308.90
$R_{I\text{-}1}$ (Ω)	26.31	31.65	32.51	34.83	39.06	46.38	23.04	70.12	78.58	48.45
CPE-$T_{I\text{-}1}$ ($Fs^{\alpha-1}$)	6.34E-07	6.32E-07	5.32E-07	1.37E-07	1.98E-07	3.06E-07	6.36E-07	1.84E-07	1.42E-07	1.00E-07
CPE-$P_{I\text{-}1}$ (α)	0.751	0.729	0.779	0.897	0.869	0.833	0.781	0.862	0.872	0.824
$C_{I\text{-}1}$ (F)	1.73E-08	1.13E-08	2.35E-08	3.36E-08	3.37E-08	3.29E-08	2.81E-08	3.03E-08	2.66E-08	7.38E-09
$R_{I\text{-}2}$ (Ω)	27.89	31.64	33.28	34.59	37.85	38.86	28.08	43.58	45.01	36.45
CPE-$T_{I\text{-}2}$ ($Fs^{\alpha-1}$)	5.48E-05	5.21E-05	5.21E-05	5.42E-05	5.17E-06	6.46E-05	5.78E-05	5.78E-05	9.89E-05	4.12E-05
CPE-$P_{I\text{-}2}$ (α)	0.521	0.512	0.512	0.514	0.521	0.512	0.497	0.493	0.472	0.517
$C_{I\text{-}2}$ (F)	1.41E-07	1.16E-07	1.22E-07	1.42E-07	1.65E-07	2.15E-08	8.74E-08	1.23E-07	2.32E-07	9.58E-08
$R_{I\text{-}4}$ (Ω)	19.65	20.64	22.17	25.16	27.61	29.31	19.07	47.24	60.35	36.48
CPE-$T_{I\text{-}4}$ ($Fs^{\alpha-1}$)	3.57E-02	5.30E-02	4.84E-02	3.10E-02	4.51E-02	4.48E-02	3.53E-02	3.53E-02	2.11E-02	4.41E-02
CPE-$P_{I\text{-}4}$ (α)	0.486	0.493	0.515	0.493	0.511	0.448	0.496	0.492	0.487	0.420
$C_{I\text{-}4}$ (F)	2.45E-02	5.81E-02	5.16E-02	2.45E-02	5.56E-02	6.26E-02	2.36E-02	5.99E-02	2.72E-02	8.50E-02

References

1 Y. J. Kim, S. Nahm, J.-H. Lee and H. Kim, *ACS Mater. Lett.*, 2025, **7**, 724–729.

2 W. D. Jung, J.-S. Kim, Y. J. Kim, H. Jeong, D. Han, K.-W. Nam, D. Ahn, D.-H. Kwon, H.-G. Jung, J.-H. Lee and H. Kim, *Adv. Funct. Mater.*, 2023, **33**, 2211185.

3 H. Jeong, H. Hwang, J.-W. Cho, D. Shin, J.-H. Lee, S. S. Shin, J.-H. Hwang and H. Kim, *J. Mater. Chem. A*, 2024, **12**, 22797–22808.

4 J. Y. Jung, H. Jeong, Y. J. Kim, S. M. Cho, Y. Jang and H. Kim, *J. Mater. Chem. A*, 2024, **12**, 12405–12411.

5 Q. Zhang, F.-H. Li, X.-X. Zhang, H.-B. Wang, F.-C. Li, Z.-Y. Guo and Z. Zhang, *J. Electrochem. Soc.*, 2021, **168**, 040522.

6 Y. Liu, H. Peng, H. Su, Y. Zhong, X. Wang, X. Xia, C. Gu and J. Tu, *Adv. Mater.*, 2022, **34**, 2107346.

7 C. Liao, C. Yu, S. Chen, C. Wei, X. Miao, S. Cheng and J. Xie, *Scripta Mater.*, 2023, **226**, 115219.

8 W. Arnold, V. Shreyas, S. Akter, Y. Li, S. Halacoglu, M. B. K. Koralalage, X. Guo, D. Vithanage, W. Wei, G. Sumanasekera, J. B. Jasinski, B. Narayanan and H. Wang, *J. Phys. Chem. C*, 2023, **127**, 11801–11809.

9 F. Zhao, J. Liang, C. Yu, Q. Sun, X. Li, K. Adair, C. Wang, Y. Zhao, S. Zhang, W. Li, S. Deng, R. Li, Y. Huang, H. Huang, L. Zhang, S. Zhao, S. Lu and X. Sun, *Adv. Energy Mater.*, 2020, **10**, 1903422.

10 Z. Zhang, C. Yu, R. Xu, L. Peng, H. Ren, J. Zhang, L. Zhang, S. Cheng and J. Xie, *Scripta Mater.*, 2022, **210**, 114475.

11 H. Raj, A. Neveu, C. Jordy, V. Pelé and V. Pralong, *Rare Met.*, 2022, **41**, 798–805.

12 G. Liu, J. Zhang, J. Yang, J. Chen, X. Xiao and X. Yao, *J. Energy Chem*., 2025, **100**, 50–58.

13 H. Yan, R. Song, R. Xu, S. Li, Q. Lin, X. Yan, Z. Wang, C. Yu and L. Zhang, *J. Energy Chem*., 2023, **86**, 499–509.

14 R. Guo, Y. Zhong, P. Yu, K. Kang, S. Li, Z. Hu, X. Wang, C. Wu and Y. Bai, *Small*, 2025, **21**, 2500764.

15 B. W. Taklu, Y. Nikodimos, H. K. Bezabh, K. Lakshmanan, T. M. Hagos, T. A. Nigatu, S. K. Merso, H.-Y. Sung, S.-C. Yang, S.-H. Wu, W.-N. Su and B. J. Hwang, *Nano Energy*, 2023, **112**, 108471.

16 C. Liao, C. Yu, L. Peng, X. Miao, S. Chen, Z. Zhang, S. Cheng and J. Xie, *Solid State Ion.*, 2022, **377**, 115871.

17 Y. Subramanian, R. Rajagopal and K.-S. Ryu, *J. Energy Storage*, 2024, **78**, 109943.

18 Z. Yu, Y. Xu, M. Kindle, D. Marty, G. Deng, C. Wang, J. Xiao, J. Liu and D. Lu, *ACS Nano*, 2024, **18**, 11955–11963.

19 Z. Wu, S. Chen, C. Yu, C. Wei, L. Peng, H.-L. Wang, S. Cheng and J. Xie, *Chem. Eng. J*., 2022, **442**, 136346.

20 R. Rajagopal and K.-S. Ryu, *Chem. Eng. J*., 2020, **402**, 126179.